www.acsnano.org

In-Plane Anisotropy in the Layered Topological Insulator Ta₂Ni₃Te₅ Investigated via TEM and Polarized Raman Spectroscopy

Kamal Harrison, Dylan A. Jeff, Jonathan M. DeStefano, Olivia Peek, Akihiro Kushima, Jiun-Haw Chu, Humberto R. Gutiérrez,* and Saiful I. Khondaker*



Downloaded via UNIV OF WASHINGTON on April 18, 2024 at 23:24:49 (UTC). See https://pubs.acs.org/sharingguidelines for options on how to legitimately share published articles.

Cite This: ACS Nano 2024, 18, 4811-4821

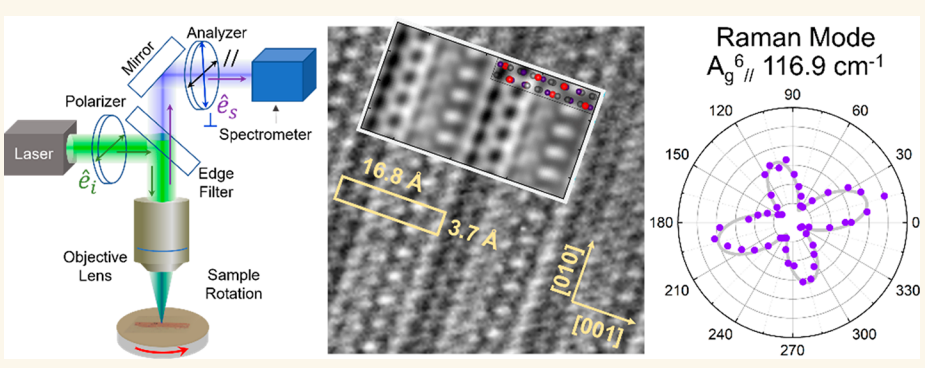


ACCESS I

III Metrics & More

Article Recommendations

s Supporting Information



ABSTRACT: Layered Ta₂M₃Te₅ (M = Pd, Ni) has emerged as a platform to study 2D topological insulators, which have exotic properties such as spin-momentum locking and the presence of Dirac fermions for use in conventional and quantum-based electronics. In particular, Ta₂Ni₃Te₅ has been shown to have superconductivity under pressure and is predicted to have second-order topology. Despite being an interesting material with fascinating physics, the detailed crystalline and phononic properties of this material are still unknown. In this study, we use transmission electron microscopy (TEM) and polarized Raman spectroscopy (PRS) to reveal the anisotropic properties of exfoliated few-layer Ta2Ni3Te5. An electron diffraction and TEM study reveals structural anisotropy in the material, with a preferential crystal orientation along the [010] direction. Through Raman spectroscopy, we discovered 15 vibrational modes, 3 of which are ultralow-frequency modes, which show anisotropic response with sample orientation varying with the polarization of the incident beam. Using angle-resolved PRS, we assigned the vibrational symmetries of 11 modes to A_g and two modes to B_{3g} . We also found that linear dichroism plays a role in understanding the Raman signature of this material, which requires the use of complex elements in the Raman tensors. The anisotropy of the Raman scattering also depends on the excitation energies. Our observations reveal the anisotropic nature of Ta2Ni3Te5, establish a quick and nondestructive Raman fingerprint for determining sample orientation, and represent a significant advance in the fundamental understanding of the two-dimensional topological insulator (2DTI) Ta₂Ni₃Te₅ material.

KEYWORDS: 2D materials, quantum materials, Raman spectroscopy, transmission electron microscopy, in-plane anisotropy, topological insulator

opological insulators (TI) have emerged as a captivating class of materials, offering a platform for exploring quantum states that could potentially revolutionize the fields of electronics, spintronics, and quantum computing. These materials possess a band gap that is topologically distinct from that of conventional insulators or semiconductors, leading to distinctive electronic properties. Materials with strong spin—orbit coupling can also host

Received: October 1, 2023 Revised: January 21, 2024 Accepted: January 23, 2024 Published: February 2, 2024





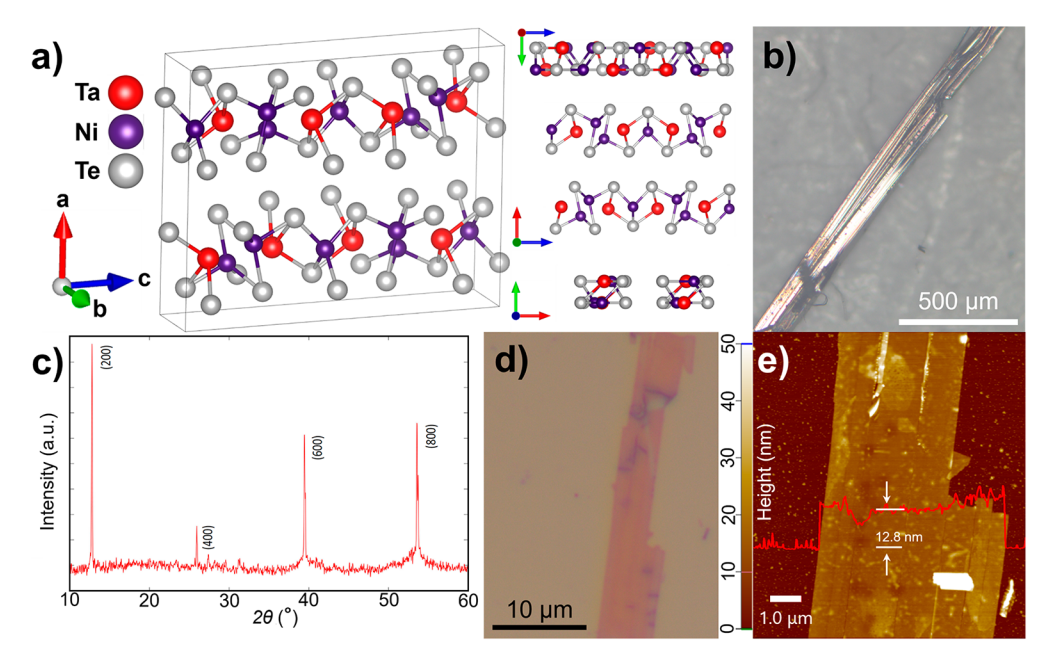


Figure 1. (a) Diagrams of the atomic structure of $Ta_2Ni_3Te_5$, including a 3D perspective and crystallographic projections along three major axes. (b) Optical image of a single crystal of the material. (c) The single-crystal X-ray diffraction spectrum taken along the $\langle 100 \rangle$ family of planes. (d) A representative optical micrograph of a flake. (e) An atomic force micrograph of the same flake showing the variations in the height profile along a horizontal line scan.

topological insulating properties with conducting surfaces⁴⁻⁶ due to the presence of gapless states on the interface between a topological insulator and a trivial insulator such as vacuum. These states are protected by time reversal symmetry resulting in spin-momentum locking where spins of opposite directions have opposite momentums. This single-direction spin filtering of electrons results in there being no available states for electron backscattering, leading to high mobilities compared to trivial semiconductors. 7,8 Within this realm of topological insulators, layered two-dimensional topological insulators (2DTIs), also known as quantum spin Hall insulators, have garnered significant interest. These materials exhibit helical edge states that behave similarly to one-dimensional conductors. The quantum spin Hall effect indicative of 2DTIs has previously been realized in quantum well structures.^{7,10} However, a layered material with 2DTI behavior has advantages compared to quantum well structures such as increased tunability and accessibility to external stimuli like light. By combining the fascinating effects of topological insulators with the tunability of 2D materials, layered 2DTIs hold the potential for innovations in nanoelectronics, facilitating the development of next-generation devices like topological field-effect transistors. 11 Therefore, the study of layered 2DTIs will aid in understanding the topological phases of matter and their potential applications in conventional and quantum-based electronics.

 $Ta_2Ni_3Te_5$ is part of a class of layered 2DTIs, $Ta_2M_3X_5$ (M=Ni, Pd; X=Se, Te), that has recently gained interest as a platform to explore topological states. Some of the materials in this class have been shown to have exotic properties such as superconductivity, excitonic states, edge states, and Luttinger liquid behavior. ^{12–17} In particular, $Ta_2Ni_3Te_5$ is also predicted to possess a second-order topology with gapless corner states, making it a quadrupole topological insulator. The double band inversion in $Ta_2Ni_3Te_5$ is expected to manifest as a band gap of 65 meV, ¹⁸ large enough to be observed at room temperature.

Moreover, $Ta_2Ni_3Te_5$ exhibits topological phase transitions under pressure and is predicted to undergo a similar phase transition in response to strain, ^{19,20} highlighting its tunability and potential for practical applications.

In addition to its topological properties, Ta2Ni3Te5 is also likely to host in-plane anisotropy due to its anisotropic crystal lattice and point group. While the majority of experimentally accessible layered materials display relatively isotropic in-plane properties, 21 anisotropic 2D materials offer an additional degree of freedom to tune properties. This can be seen in black phosphorus, where the crystal orientation changes its optical, electronic, and thermal properties, allowing for anisotropic photoelectric and thermoelectric devices.^{22–2} Therefore, the in-plane anisotropy in Ta2Ni3Te5 introduces an additional degree of freedom, enabling the exploration and manipulation of next-generation electrical, optical, and thermal devices. 22,25 Despite being an interesting material with many exotic properties, experimental investigations of the exfoliation, anisotropic properties, atomic structures, and optical and vibrational properties of the 2DTI Ta2Ni3Te5 including the number of phonon modes and their symmetry assignments have not yet been studied. Such studies are significant in advancing the fundamental understanding of layered topological anisotropic materials for the realization of many overarching goals in future applications.

In this work, we present the anisotropic structural and phononic properties of exfoliated few-layer $Ta_2Ni_3Te_5$ flakes. X-ray diffraction (XRD) of the bulk crystal, grown through iodine-assisted vapor transport, shows a good crystallinity of the material. Optical and atomic force microscopy (AFM) images of the exfoliated flakes show an elongated nanoribbon-like morphology. A high-resolution transmission electron microscopy (HRTEM) investigation reveals the anisotropic nature of the crystal with $a=13.91, b=3.7\pm0.6$, and $c=16.8\pm0.6$ Å. Due to the structural anisotropy, elongated ribbon-like shapes are formed in the exfoliated samples whose

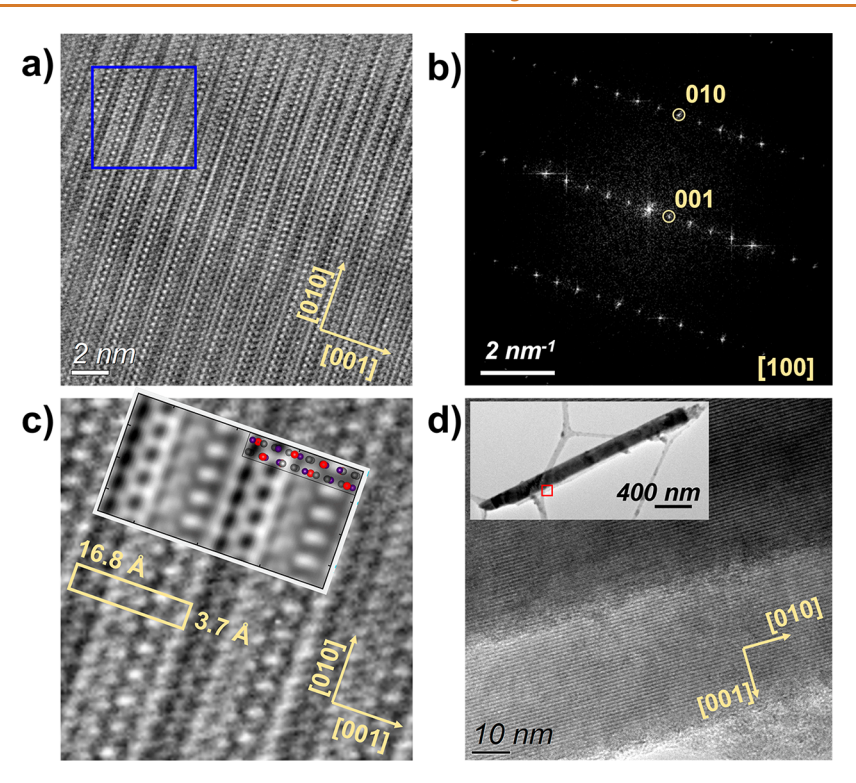


Figure 2. TEM images of $Ta_2Ni_3Te_5$ showing (a) a HRTEM image of the anisotropic crystal lattice, (b) the Fourier transform of the image with the corresponding reciprocal lattice vectors labeled, and (c) higher magnification HRTEM of $Ta_2Ni_3Te_5$, from the region in (a) highlighted in blue. The inset contains a simulated TEM image and the unit cell as seen from the [100] crystallographic direction. The measured lattice parameters along the [010] and [001] directions are 3.7 ± 0.6 and 16.8 ± 0.6 Å, respectively. (d) TEM image of ribbon edge (red square region in the inset) showing that the (001) planes are parallel to the edge and hence the ribbon longest dimension extends along the [010] crystalline direction. This was confirmed to be the case in all the ribbons examined.

preferential crystal orientation was determined, by TEM, to be along the [010] direction. Using angle resolved polarized Raman spectroscopy (ARPRS), we discovered 15 phonon modes, 3 of which are ultralow-frequency (ULF) modes, likely to be shear and breathing modes. We assigned 11 of these modes to $A_{\rm g}$ vibrational symmetry and 2 modes to $B_{\rm 3g}$. We also discuss complex tensor analysis and the excitation energy dependence of the Raman data.

RESULTS AND DISCUSSION

Unlike most layered 2D materials, Ta2Ni3Te5 hosts a large and rather complex unit cell. Each unit cell contains 40 atoms with two monolayers of 20 atoms each, with van der Waals interactions between the layers.²⁰ The crystal lattice of Ta2Ni3Te5 is predicted to be orthorhombic with point group D_{2h} and space group *Pnma* (Figure 1a). For this study, single crystals of Ta₂Ni₃Te₅ were grown via an iodine vapor transport method as outlined in Methods. A representative single crystal is shown in Figure 1b. These crystals grow as shiny ribbons that are as long as 2 mm and as wide as 200 μ m. The single-crystal XRD taken on a grown sample that is presented in Figure 1c shows good crystallinity with only (h00) planes present due to monolayers that extend in the (100) plane. Using XRD analysis we obtain 13.91 Å as the lattice constant for a, consistent with previously reported values. 28,30 Mechanical exfoliations via the "Scotch tape" method were then performed to obtain few-layer samples, a representative optical micrograph of which is shown in Figure 1d. Exfoliated Ta₂Ni₃Te₅ flakes are much more transparent than their bulk counterparts, appearing red on a Si substrate

with a 250 nm oxide capping layer. Exfoliated flakes mirror the elongated ribbon shape of the bulk crystals. The AFM image in Figure 1e shows a height profile where the thickness of the flake is 12.8 nm (18 layers); however, along the line profile the height can vary between 9.8 nm (~14 layers) and 19.6 nm (~30 layers) (see Figure S1a). This thickness variation along the ribbon is due to the inherent randomness of the exfoliation process. Additional exfoliated flakes are presented in Supporting Figure S1 and show thicknesses from 8.0 to 19.0 nm. Notice that the interlayer distance is a/2 = 6.955 Å as obtained from the XRD analysis. We note that the mechanical exfoliation of Ta₂Ni₃Te₅ was not reported before. Not all layered materials can be easily exfoliated due to the different strengths of the interlayer attractions; the viability of exfoliating Ta2Ni3Te5 could facilitate many future studies on this material.

Transmission Electron Microscopy. HRTEM imaging and diffraction pattern analysis were performed to investigate the atomic structure of Ta₂Ni₃Te₅. Flakes used for TEM imaging were exfoliated via sonication, as outlined in Methods. The sonication produced an elongated morphology similar to the exfoliated flakes in Figure 1 but generated smaller flakes than those obtained by the "Scotch tape" method. Different scanning electron microscopy (SEM) images of sonicated flakes are provided in Supporting Figure S2. The solution containing exfoliated ribbons was deposited on TEM grids, and the thinnest flakes were used to perform TEM analysis. Figure 2a shows an atomic-resolution HRTEM image of one nanoribbon, where the anisotropic nature of the crystal lattice is revealed. Figure 2b shows the Fourier transform corresponding to the HRTEM image in Figure 2a with the

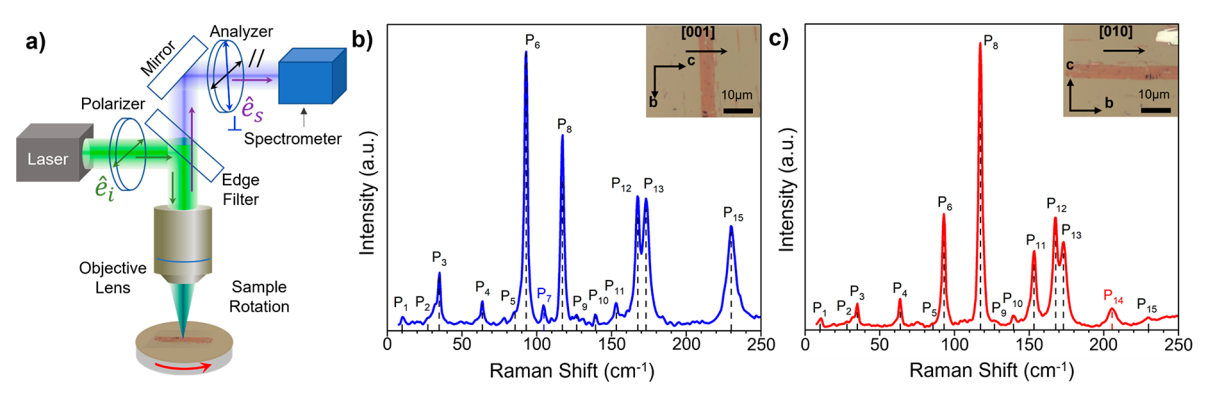


Figure 3. (a) Diagram of the experimental setup for the angularly dependent Raman intensity with sample rotation (θ) with respect to the incident beam. Raman spectra of $Ta_2Ni_3Te_5$ with the polarization of the incident laser along the (b) [001] and (c) [010] crystal directions, including the ultralow-frequency region.

Table 1. Raman Tensors for the D_{2h} Point Group

mode	all	A_{g}	B_{1g}	B_{2g}	B_{3g}
R	$\begin{pmatrix} a & d & e \\ d & b & f \\ e & f & c \end{pmatrix}$	$\begin{pmatrix} a & 0 & 0 \\ 0 & b & 0 \\ 0 & 0 & c \end{pmatrix}$	$\begin{pmatrix} 0 & d & 0 \\ d & 0 & 0 \\ 0 & 0 & 0 \end{pmatrix}$	$\begin{pmatrix} 0 & 0 & e \\ 0 & 0 & 0 \\ e & 0 & 0 \end{pmatrix}$	$ \begin{pmatrix} 0 & 0 & 0 \\ 0 & 0 & f \\ 0 & f & 0 \end{pmatrix} $

lattice vectors labeled. Using the Fourier transform (FT) we have obtained the remaining lattice constants of $Ta_2Ni_3Te_5$, which are 3.7 \pm 0.6 and 16.8 \pm 0.6 Å along the directions b = [010] and c = [001], respectively; the uncertainties used for these values correspond to the maximum deviation from the average value as shown in Supporting Figure S3.

Figure 2c provides a larger magnification of the region enclosed in the blue square of Figure 2a. The simulated image in the inset of Figure 2c matches the actual image well and allows for a correlation between the light and dark features in the image and the atomic positions in the unit cell. More information on the TEM simulation used in this study is shown in Supporting Figure S4. Here the direct measurement, in real space, of the unit cell also reveals the in-plane lattice parameters with values very close to those obtained from the FT. The ribbon's longest dimension (or ribbon axis) extends along the [010] crystalline direction. This is apparent in Figure 2d, which shows a lower magnification TEM image of a Ta2Ni3Te5 nanoribbon's edge. These results are consistent among the three nanoribbons analyzed by using TEM. Even at this magnification, the (001) planes can be observed to be parallel to the nanoribbon axis along the [010] direction. The elongated morphology of the grown crystals suggests distinct growth rates along the different directions in this highly anisotropic crystal lattice, and the cleavage along the [010] direction to form the nanoribbons during exfoliation indicates weaker bond strengths in the [001] direction.

Raman Spectrum of $Ta_2Ni_3Te_5$. We further investigated the in-plane anisotropy of $Ta_2Ni_3Te_5$ through a series of polarized Raman spectroscopy experiments in backscattering geometry. We performed different Raman scattering experiments where the relative orientations of the incident electric field polarization (\hat{e}_i) , the scattered polarization (\hat{e}_s) , and the crystallographic orientation of the sample were varied. Although a general schematic for the experimental setup is shown in Figure 3a, not all of the optical elements (polarizer, half-wave plate, and analyzer) were used simultaneously in all of the experiments, as we describe next.

In our first experiment (Figure 3), $\hat{\epsilon}_i$ is fixed in the horizontal direction using a polarizer, and the Raman spectra were

collected for the Ta2Ni3Te5 ribbon oriented perpendicular (inset in Figure 3b) and parallel (inset in Figure 3c) to this direction, so we are only probing the effect of \hat{e}_i being oriented along the [010] or [001] crystalline direction. In both spectra, we observed common peaks at 10, 28, 35, 63, 86, 92, 116, 127, 138, 153, 166, 172, and 228 cm⁻¹. The peak at 104 cm⁻¹ is only observed when the laser is linearly polarized in the [001] crystal direction, while the peak at 204 cm⁻¹ is observed for the other configuration (\hat{e}_i along the [010] direction). The spectra in Figure 3 were taken with a long acquisition time of 60 s, which allowed us to observe the low-intensity peaks. The ultralow-frequency (ULF) Raman peaks observed in Figure 3 at 10, 28, and 34 cm⁻¹ are usually associated with breathing and/or shear modes in van der Waals layered systems. 31,32 It is worth noting that the intensity of the Raman peaks for Ta₂Ni₃Te₅ depends on the orientation of the crystal, which could be due to the anisotropic nature of the crystal structure shown in our TEM analysis. For example, the peak intensity at 204 cm⁻¹ is higher when the incident laser is polarized along the [001] crystal direction, while the peak at 228 cm⁻¹ is more intense when the laser is polarized along the [010] crystal direction. The orientation response of some of these peaks facilitates identification of the crystal orientation by manipulating the relative polarization of the light. To do so, we can use the Raman peaks at 92 and 116 cm⁻¹ which have the highest overall intensities and the Raman peaks at 204 and 228 cm⁻¹ which have the highest and lowest anisotropic behavior, respectively. When the laser polarization is along the [001] crystal direction, we observe a peak intensity ratio of $\frac{P_6}{P_c} = 1.42$ and $\frac{P_{14}}{P_{15}} = 0.06$, while in the [010] crystal direction these ratios change to $\frac{P_6}{P_8} = 0.38$ and $\frac{P_{14}}{P_{15}} = 2.02$. The anisotropy of the Raman response in Ta₂Ni₃Te₅ can be understood through the Raman tensors of point group D_{2h} shown in Table 1.³³ The Raman tensor elements of this material are given by the derivative of the dielectric tensor. Depending on the point group of the material, the tensor's elements have different

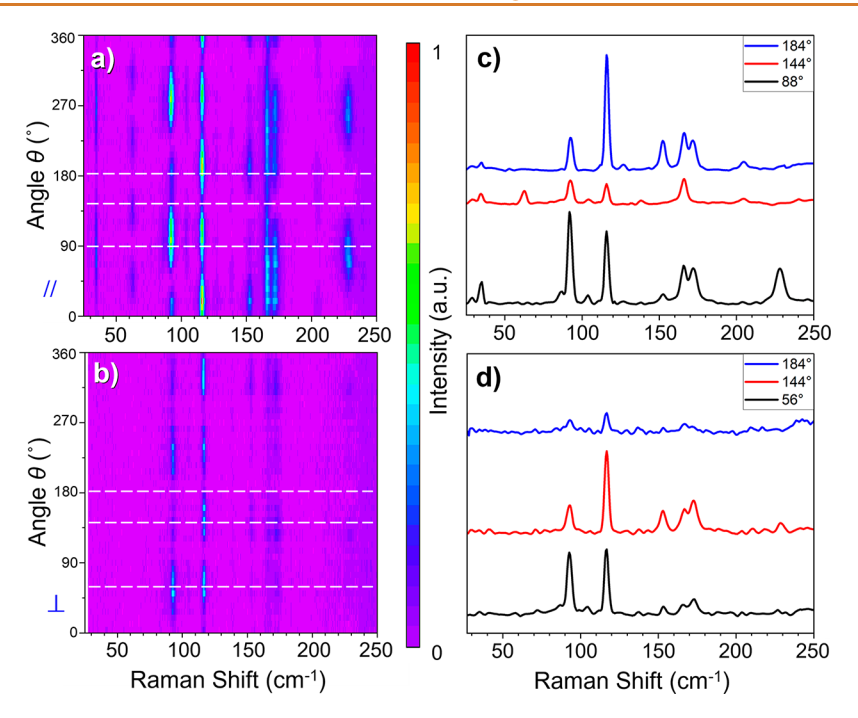


Figure 4. Color maps for the angular dependence of the Raman intensity spectra measured in the (a) parallel and (b) cross-polarization configurations. (c, d) Raman spectra along the white dashed lines in (a) and (b), respectively.

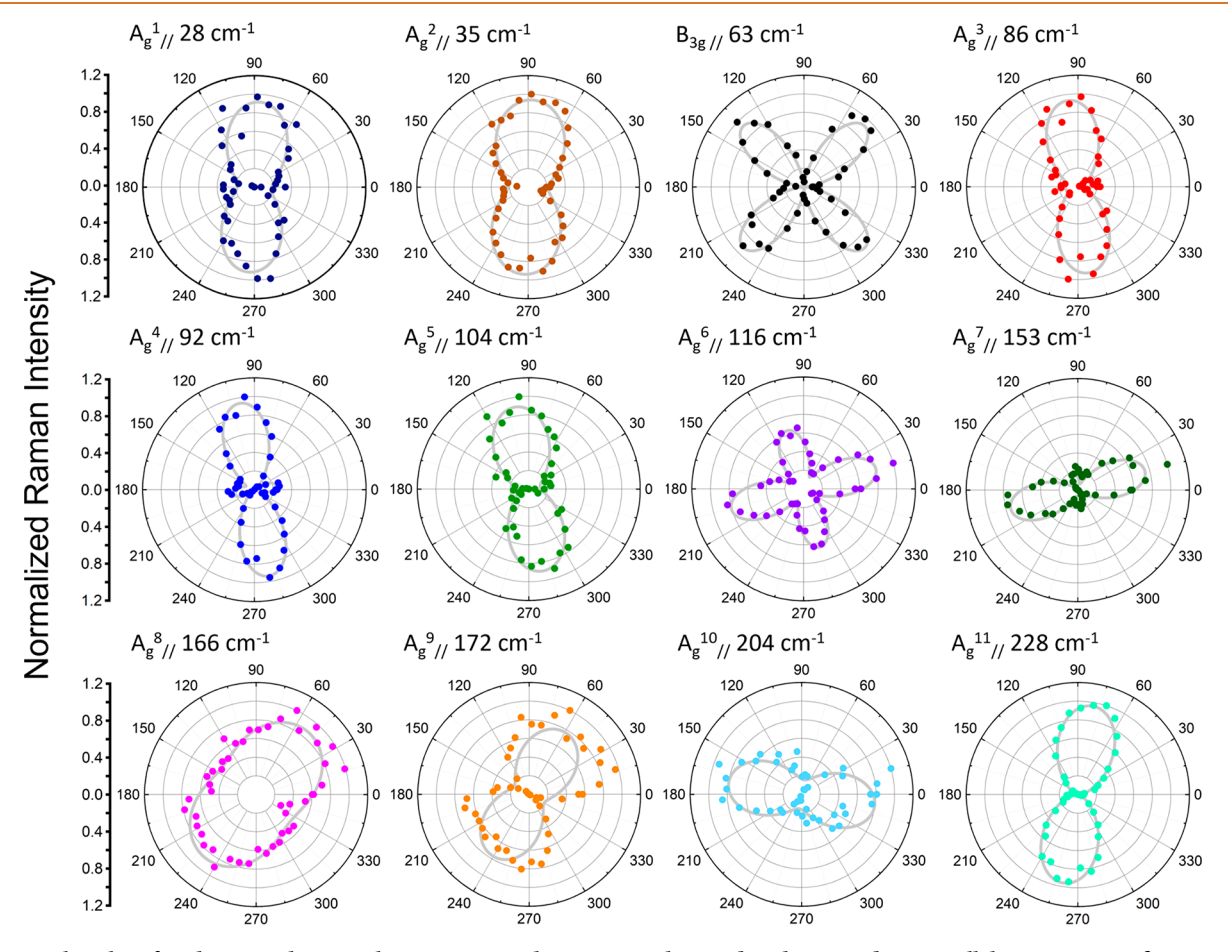


Figure 5. Polar plots for changing the crystal orientation with respect to the incident beam under a parallel scattering configuration. The intensities are normalized intensities, and the angle used is the angle between the polarization of the laser and the [010] crystal direction, which we notate by θ . Experimental data are represented as dots, while fittings, using eq 4 for the B_{3g} mode and eq 8 for the A_g modes, are represented as solid curves.

values and hence different optical and electronic properties along those directions.

 $Ta_2Ni_3Te_5$ has 120 eigenmodes at the Γ point of the Brillouin zone predicted through group theory, ³³ including 3 acoustic and 117 optical modes, which can be displayed as

$$\Gamma = 20A_g + 10B_{1g} + 20B_{2g} + 10B_{3g} + 10A_u + 19B_{1u}$$
$$+ 9B_{2u} + 19B_{3u} + (B_{1u} + B_{2u} + B_{3u})_{acoustic}$$

where A_g , B_{1g} , B_{2g} , and B_{3g} are Raman-active modes. Of the 60 Raman-active modes, only the 30 modes from A_g and B_{3g} are observable in the backscattering geometry, as we discuss next based on tensor analysis. The next series of experiments are performed to identify which of the observed peaks presents A_g and B_{3g} symmetries.

Angular Dependence of the Raman Peak Intensities. In a second experiment, we systematically varied the relative orientations of \hat{e}_i and \hat{e}_s with respect to the crystal to investigate the effect of the anisotropic crystal structure of Ta₂Ni₃Te₅ on the Raman spectrum. With this aim, we introduced a polarizer, an analyzer, and a rotation stage in which the sample was mounted, as indicated in Figure 3a. The spectrum was measured as a function of the sample rotation angle (θ) when \hat{e}_i and \hat{e}_s are parallel (Figure 4a) and perpendicular (Figure 4b) to each other. The resulting color maps for each configuration are shown in Figure 4a,b, where θ is the angle between the polarization of the incident laser (\hat{e}_i) and the [010] crystal direction. Spectra at three representative angles of each configuration are also shown in Figure 4c,d, respectively. Figure 5 shows the polar plots for some of the peaks in the parallel-polarization configuration in Figure 4a. The Raman peaks at 28, 35, 86, 92, 104, and 228 cm⁻¹ have 2fold symmetry (two-lobed shape) with maximum intensities close to 90°, while the Raman peaks at 153 and 204 cm⁻¹ have 2-fold symmetry with the two lobes of maximum intensity oriented close to the 0° angle. Only two peaks (63 and 116 cm⁻¹) show clear 4-fold symmetry. However, while the peak at 63 cm⁻¹ has its four lobes rotated 45° from the vertical and horizontal axis, the peak at 116 cm⁻¹ has its four lobes oriented closer to the axis. Meanwhile, the Raman peaks at 166 and 172 cm⁻¹ display angle-dependent intensities with low or no symmetry. For the cross-polarization configuration, the overall absolute intensity of the spectra decreased significantly and fewer peaks were observed. These include the peaks at 92, 104, 116, 153, 166, 172, and 228 cm⁻¹.

To quantitatively fit the data, we utilize the equation for the polarization-dependent intensity (I) of each Raman-active mode

$$I \propto |\hat{\mathbf{e}}_{\mathbf{i}} \cdot \mathbf{R} \cdot \hat{\mathbf{e}}_{\mathbf{s}}|^2 \tag{1}$$

where \hat{e}_i and \hat{e}_s are the unit vectors associated with the polarization of the incident and scattered electric fields, respectively, and **R** is the Raman tensor corresponding to each mode given in Table 1.³³ In this particular experiment where the sample is rotated while keeping the polarization fixed, we can write the unit vectors as a function of the angle θ with respect to the [010] crystal axis as follows: $\hat{e}_i = (0, \cos \theta, \sin \theta)$ for both parallel- and cross-polarization configurations, while $\hat{e}_s = (0, \cos \theta, \sin \theta)$ for parallel-polarization and $\hat{e}_s = (0, -\sin \theta, \cos \theta)$ for cross-polarization. The incident and scattered light propagate along the x-axis (parallel to vector \vec{a} in Figure 1a). Utilizing the Raman tensors shown in Table 1, we obtain the angular dependence of the intensities of the A_{σ}

 (I_{A_g}) and B_{3g} $(I_{B_{3g}})$ modes (see section S12 in the Supporting Information for the derivation):

$$I_{A_g}^{\parallel} \propto [c(\sin^2 \theta) + b(\cos^2 \theta)]^2$$
 (2)

$$I_{A_g}^{\perp} \propto [(c - b)(\cos \theta \cdot \sin \theta)]^2$$
 (3)

$$I_{\mathrm{B}_{3\mathrm{g}}}^{\parallel} \propto \left[2f(\cos\theta \cdot \sin\theta)\right]^2$$
 (4)

$$I_{\mathsf{B}_{\mathsf{3}_{\mathsf{K}}}}^{\perp} \propto [f\cos 2\theta]^2 \tag{5}$$

For parallel-polarization, eq 2 assigns a 2-fold symmetry to the A_g modes that varies with the ratio of the tensor elements b/c(Supporting Figure S6a). The intensities of the modes with c >b peaks dominate when the incident laser is polarized in the [001] crystal direction. Conversely, the modes with b > c peaks dominate when the laser is polarized in the [010] crystal direction. On the other hand, according to eq 4, the B_{3g} modes are expected to have a 4-fold symmetry (four-lobed clover shape) with the lobes of maximum intensity rotated 45° from the horizontal and vertical axes (Supporting Figure S6c). The peak at 63 cm⁻¹ is in good agreement with B_{3g} symmetry. Additionally, the peak at 138 cm⁻¹ presents very low intensity and hence its polar plot is more scattered (Supporting Figure S7c); however, the position of its local maxima is also consistent with the B_{3g} symmetry. The intensities for the B_{1g} and B_{2g} symmetries, calculated according to eq 1, are zero; hence, they are not observed for this scattering configuration. For the cross-polarization condition, eq 3 predicts 4-fold symmetry for the A_g vibrational modes (similar to the B_{3g} in parallel-polarization), but the maximum intensity varies depending on the b/c ratio (Figure S6b). The above analysis, which uses real Raman tensors, can describe the angular dependence of the B_{3g} modes. However, not all of the peaks resembling the A_g symmetry can be well fitted by these equations (see section S7 in the Supporting Information).

Next, we consider introducing complex tensor elements to understand the effect of light absorption on the angle-dependent Raman intensity of some of these modes. This is due to birefringence which changes the absorption of light within the material for different directions and polarizations. The complex tensor elements corresponding to (a, b, c, and f) in Table 1 can be written as $(|a|e^{i\phi a}, |b|e^{i\phi b}, |c|e^{i\phi c}, |f|e^{i\phi f})$, respectively, where $\phi = \tan^{-1}\frac{R_{ij}}{R_{ij}}$ for each element of the Raman tensor (R). Substituting the real by the complex tensor elements (section S12 in the Supporting Information) eqs 2 and 3 can be rewritten as

$$I_{\rm A_g}^{\parallel} \propto [lc {\rm sin}^2 \theta + lb {\rm lcos}^2 \theta \cos \phi_{bc}]^2 + lb {\rm l}^2 \cos^4 \theta \sin^2 \phi_{bc}$$
 (6)

$$I_{\mathrm{A_g}}^{\perp} \propto \left[(|c| - |b| \cos \phi_{bc})^2 + |b|^2 \sin^2 \phi_{bc} \right] \sin^2 \theta \cos^2 \theta \tag{7}$$

It is important to notice that the use of complex tensor elements does not affect the angle-dependent intensity for the B_{3g} modes, hence eqs 4 and 5 remain the same but have the absolute value |f| instead of f. For the A_g modes, eqs 6 and 7 can now explain the formation of secondary local maxima for some of the Ag-like modes; for instance, the 92 cm⁻¹ peak has the two lobes of absolute maxima oriented in the vertical direction (along 90 and 270°) but has secondary maxima at 0

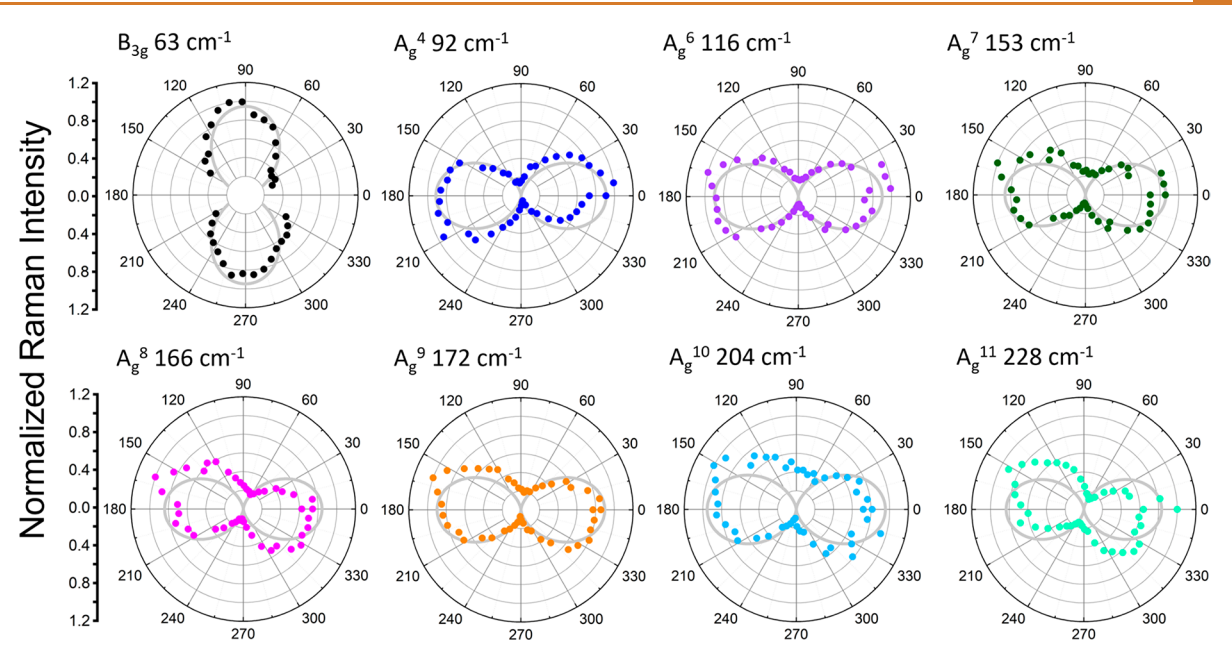


Figure 6. Polar plots for changing the polarization of the incident beam, with respect to the polarization of the analyzer. The intensities are normalized intensities and the angle used is the angle between the polarization of the incident and scattered light, which we notate by φ . Experimental data are represented as dots, while fits are represented as solid curves.

and 180°. In contrast, for the peaks at 116, 127, and 153 cm⁻¹ the secondary maxima are close to 90 and 270° instead. However, for some of the A_g -like peaks, the angular position of the intensity maxima presents a small deviation from those predicted by tensor analysis along the main crystallographic axes. Since this angular deviation (or shift) varies for the different peaks, it cannot be associated with a systematic error in the alignment between the laser polarization and crystal axis for $\theta=0$. To better fit the experimental data, we artificially introduced the aforementioned angular shift as φ , and with this small correction eqs 6 and 7 can now be written as

$$I_{A_g}^{\parallel} \propto \left[|c| \sin^2 (\theta + \varphi) + |b| \cos^2 (\theta + \varphi) \cos \phi_{bc} \right]^2 + |b|^2 \cos^4 (\theta + \varphi) \sin^2 \phi_{bc}$$
(8)

$$I_{A_g}^{\perp} \propto \left[(|c| - |b| \cos \phi_{bc})^2 + |b|^2 \sin^2 \phi_{bc} \right] \sin^2(\theta + \varphi)$$

$$\cos^2(\theta + \varphi) \tag{9}$$

At this moment, the origin of the small shifts φ is not completely understood for Ta₂Ni₃Te₅ and will require further studies, where the thickness and excitation laser are systematically varied. However, similar angular deviations of the Raman intensity maxima from the main crystallographic axes have been also reported for ReS₂.^{37,38} In this case, the angular deviation also depends on the thickness and the excitation laser energy and is attributed to the appearance of a nonzero offdiagonal Raman tensor and phase delay. The Raman selection rules are governed by the polarization-dependent electronphoton and electron-phonon interactions. For the A_o modes, the symmetry of the optical transitions, and hence the electron-photon interactions, should be the same. However, the electron-phonon interactions could vary for each A_g mode, serving as the origin of the different polar plots observed in Figure 5.3

Using eq 4 for the B_{3g} mode and eq 8 for the A_g modes, we fitted the data in Figure 5 and obtained the ratios of tensor

elements b and c, as well as the complex phase difference $\phi_{bc} = \phi_b - \phi_c$ and the angular shift φ for each Raman peak. The values of the fitting parameters using the different equations are summarized in sections S6–S8 in the Supporting Information. The 172, 204, and 228 cm⁻¹ modes had small complex phase differences ϕ_{bc} , as calculated by eq 8. However, the modes at 92, 116, and 153 cm⁻¹ had complex phase differences of around 120°, which are comparable to those of other materials, where a considerable absorption effect is seen. ^{34,38,39}

To further verify the peak assignments, a different experiment, where the sample orientation and the polarization of the scattered light are fixed, was performed. Then, using the half-wave plate in the setup described above, the polarization of the incident light was systematically rotated by α . The polar plots (dots) in Figure 6 correspond to the angle-dependent intensities of the seven strongest peaks. For the case in which \hat{e}_i (for $\alpha=0$) and \hat{e}_s are along the [001] crystal direction, we made $\hat{e}_i=(0,\sin\alpha,\cos\alpha)$ and $\hat{e}_s=(0,0,1)$. If they are along the [010] crystal direction, then $\hat{e}_i=(0,\cos\alpha,\sin\alpha)$ and $\hat{e}_s=(0,1,0)$. Substituting these polarization vectors and R (from Table 1) in eq 1 we obtain the following relations for the angle-resolved polarized Raman intensities in this experiment:

$$I_{A_g}^{[010]} = (b \cdot \cos \alpha)^2 \tag{10}$$

$$I_{A_g}^{[001]} = (c \cdot \cos \alpha)^2 \tag{11}$$

$$I_{\mathrm{B}_{\mathrm{3g}}} = (f \cdot \sin \alpha)^2 \tag{12}$$

From these equations, we note that the polar plots corresponding to the A_g and B_{3g} modes both have 2-fold symmetry, with a 90° phase difference. The A_g modes have the two lobes of highest intensities aligned horizontally ($\alpha = 0$ and 180°), while the B_{3g} modes have two vertical lobes of high intensities ($\alpha = 90$ and 270°). The difference in values for Raman elements b and c leads to the anisotropic response of the Raman signal for light polarized in different crystal

orientations, as discussed earlier. The intensities for A_g in cross-polarization and B_{3g} in parallel-polarization modes are I=0. Hence, A_g modes are forbidden under cross-scattering while B_{3g} modes are forbidden under parallel scattering for both crystal axes. In this experiment, however, the intensity of some of the modes that we identified as A_g is considerably reduced under the cross-polarization conditions (Figure 6) but does not become completely zero likely due to the birefringence contribution and the anomalous angular shift ϕ that we observed in Figure 5.

Correlating the results in Figure 6 and those in Figure 5, the Raman peaks at 92, 116, 153, 204, and 228 cm⁻¹ are confirmed as A_g vibrational modes. The Raman peak at 63 cm⁻¹ is confirmed as a B_{3g} vibrational mode. Also, in this experiment, the peak at 138 cm⁻¹, despite having rather scattered data due to its low intensity, presents an angular intensity distribution close to that expected from a B_{3g} mode (section S10 in the Supporting Information). We tentatively assign the Raman peaks at 166 and 172 cm⁻¹ to A_o symmetry, both of which have unusual behavior in Figure 5. Using the data from Figure 5, we are also able to assign the ultralow-frequency peaks at 28 and 35 cm^{-1} and the low-intensity modes at 86 and 104 cm⁻¹ to A_g symmetry. We have analyzed additional low-intensity peaks and provided them in section S10 of the Supporting Information. The tentative assignment of vibrational symmetries to their respective Raman modes is shown in Table 2.

Table 2. Assignment of Vibrational Symmetries

mode	node peak position (cm ⁻¹)		
A_{g}	28, 35, 86, 92, 104, 116, 153, 166, 172, 204, 228		
B_{3g}	63, 138		
unknown	10, 127		

It is worth noting that some of the peaks cannot be properly fitted even by introducing complex tensor elements. There are two peaks (at 138 and 204 cm $^{-1}$) that present relatively scattered angular patterns; we believe that the main reason for this behavior is the low signal-to-noise ratio of the peaks. On the other hand, the peak at 228 cm $^{-1}$ can be fitted very well using eq 8 corresponding to the $A_{\rm g}$ modes for the experiment in Figure 5; however, Figure 6 presents a small angle deviation with respect to the angular pattern predicted by eqs 10 and 11. In contrast, the peak at 172 cm $^{-1}$ is tentatively assigned to an $A_{\rm g}$ mode based on its two-lobed angular dependence shown in Figure 6, which can be well fitted by eqs 10 and 11. However,

in the experiment corresponding to Figure 5, this peak displays an anomalous butterflylike angular pattern that cannot be accurately fitted using the tensor analysis presented here. As we mentioned earlier, similar anomalous angular rotations and butterfly patterns have been observed in ReS₂, which is another anisotropic 2D material.³⁷ In this case, the anomalous behavior was explained by the existence of nonzero off-diagonal tensor elements combined with an optical birefringence effect, which can depend on both the thickness of the sample and the excitation laser.

Excitation-Dependent Raman Spectroscopy. Next, we study Raman scattering as a function of the excitation laser energy. First-order Raman scattering is a process that involves an electronic transition between two states (that can be virtual or allowed) due to the absorption of a photon and the subsequent absorption or emission of a phonon due to the interaction of the excited electron with the lattice vibrations. The closer the excitation laser energy is to an allowed electronic transition, or excitonic state, the higher the Raman intensity is since it is close to a resonant condition. 40 The same argument is valid for higher-order Raman scattering which involves multiple phonons. 14,41 Figure 7 shows the Raman spectra for excitation energies of 1.58 eV (785 nm), 1.96 eV (633 nm), 2.33 eV (532 nm), 2.62 eV (473 nm), and 3.06 eV (405 nm), with polarizations parallel to both the [010] and [001] crystal directions. For 3.06 eV no Raman signal was observed in any polarization configuration, indicating that this energy is far from any resonant condition. Although different peaks can be observed at all of the remaining energies, 2.33 eV is the only energy for which all of the peaks are clearly observed. The Raman mode at 63 cm⁻¹ was only discernible at 2.33 and 2.62 eV excitations. Similar behavior can be seen in the peak at 104 cm⁻¹, which shows stronger coupling to the excitations at 1.58 and 2.62 eV than what is seen in the other excitations. The intensity anisotropy of the A_{σ} modes is a function of the excitation energy. This is evident in Figure 7c, where the ratio of the intensities along the two crystal directions for each Raman mode is plotted as a function of the excitation energy. The preferred polarization direction of the Raman mode at 92 cm⁻¹ switches from being c-dominant in the 1.58, 2.33, and 2.62 eV excitations to being b-dominant in the 1.96 eV excitation. This points to the anisotropy of each mode being dependent on the coupling between phonons and the electronic bands which are highly anisotropic in nature. 18 The opposite effect occurs with the Raman mode at 116 cm⁻¹ in the 1.96 eV excitation, which switches from being b-

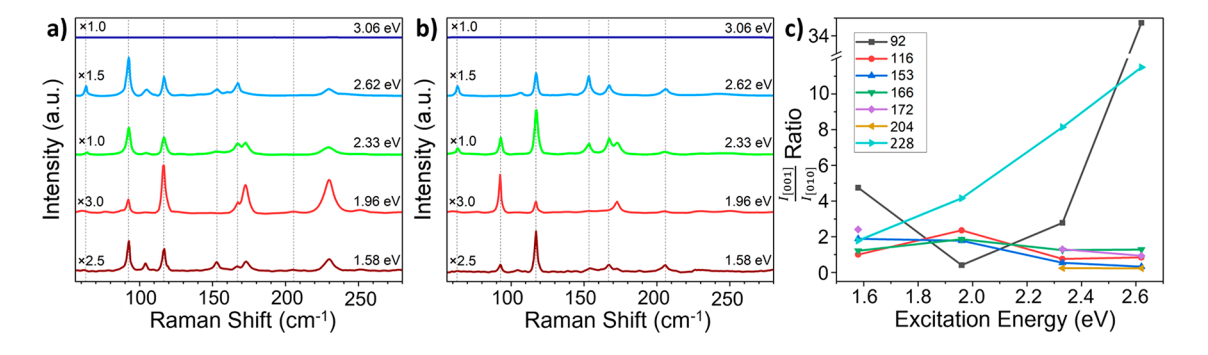


Figure 7. Raman resonance effect in $Ta_2Ni_3Te_5$ for 5 different excitation energies shown for incident laser polarization parallel to the (a) [001] and (b) [010] crystal directions. Ratios for peak intensities along the two crystal directions $\frac{I_{[001]}}{I_{[010]}}$ for each mode as a function of excitation energy (c).

dominant in the 1.58, 2.33, and 2.62 eV excitations to being c-dominant in the 1.96 eV excitation. The Raman peak at 153 cm⁻¹ gradually changes from being c-dominant to b-dominant in this range, crossing the threshold of $\frac{I_{[001]}}{I_{[010]}} = 1$ between 1.96 and 2.33 eV.

CONCLUSION

Through a comprehensive study involving XRD, AFM, TEM, and polarized Raman spectroscopy, we have established a clear correlation between the structural and optical in-plane anisotropies in exfoliated few-layer Ta2Ni3Te5. Electron diffraction and TEM analysis revealed lattice constants a =13.91, $b = 3.7 \pm 0.6$, and $c = 16.8 \pm 0.6$ Å for the material. Due to the structural anisotropy, elongated ribbon-like shapes are formed in the exfoliated samples whose preferential crystal orientation was determined, by TEM, to be along the [010] direction. This shape-structure relation was subsequently correlated with the phononic anisotropy, providing an optical signature for quick and nondestructive determination of the crystal orientation in larger area samples or devices. This method will facilitate the study and discovery of the physical properties associated with the anisotropic structure of this material. Through Raman spectroscopy, we discovered 15 vibrational modes, three of which are ultralow-frequency modes likely to be shear and/or breathing modes. The vibrational symmetries of 11 A_{g} and 2 $B_{3\text{g}}$ phonon modes in Ta₂Ni₃Te₅ were assigned also using different configurations of ARPRS. Our analysis revealed that linear dichroism plays a role in understanding the Raman signature of this material, which requires the use of complex elements in the Raman tensors. Additionally, the resonant Raman effect was leveraged to gain insight into the coupling of phonons to excited states, which revealed the intensity anisotropy as a function of the excitation energy. Our observations reveal the promise Ta₂Ni₃Te₅ has as an in-plane anisotropic layered material and significantly advance the fundamental understanding of the layered topological insulator Ta₂Ni₃Te₅.

METHODS

Single crystals of $Ta_2Ni_3Te_5$ were grown using an iodine vapor transport method as previously reported for $Ta_2Pd_3Te_5^{\ 12}$ and $Ta_2Ni_3Te_5^{\ 20}$. Ta powder (99.98%), Ni powder (99.996%), and Te powder (99.999%) were mixed in a 4:6:9 molar ratio and then loaded with a small amount of I_2 powder (99.99%) into a quartz tube which was then vacuum-sealed. The tube was heated to 500 °C in 7 h and held at this temperature for 24 h. Then the source (sink) side of the tube was heated to 900 °C (850 °C) in 8 h and held at this temperature for 96 h. The furnace was then turned off, and single crystals of $Ta_2Ni_3Te_5$ were found on the sink side of the tube. The stoichiometry of the crystals was confirmed with energy-dispersive X-ray spectroscopy using a Sirion XL30 scanning electron microscope, and the crystal structure was confirmed with single-crystal X-ray diffraction using a Rigaku MiniFlex 600 system with a Cu source and Hy-Pix 400MF 2D-detector.

Few-layer Ta₂Ni₃Te₅ flakes were obtained by mechanically exfoliating bulk crystals onto silicon wafers coated with a 250 nm SiO₂ capping layer using Nitto tape. Optimal flakes were selected based on color contrast and transparency using optical microscopy, and their thickness and layer number were determined with atomic force microscopy taken on a Park Systems NX20 instrument in noncontact mode.

SEM images were taken in a Zeiss ULTRA-55 instrument with Schottky field emission gun (voltage range: 0.1-30~kV). The image resolutions were 1 nm at 15 kV and 1.7 nm at 1 kV.

Transmission electron microscopy (TEM) analysis was conducted using an FEI Tecnai F30 instrument operated at 300 kV acceleration voltage. The sample was prepared by drop-casting. The $\rm Ta_2Ni_3Te_5$ flakes were dispersed in IPA and sonicated for 30 min. A small drop of the solution was placed on a lacey-carbon grid and dried in air for imaging. TEM image simulation was performed using QSTEM software. Here, a 2 \times 5 \times 2 supercell was used with the zone axis set to [100], corresponding to a thickness of $\sim\!\!30$ nm. The acceleration voltage and spherical and chromatic aberration were set to 300 kV, 1.2 mm, and 2.0 mm, respectively, which were taken from the specifications of the TEM used in this work (Tecnai F30). The defocus value (-80 nm) was adjusted to match the HRTEM image obtained from the experiment.

Raman experiments were conducted by using a Horiba Scientific LabRAM HR Evolution system with backscattering geometry. A 2.33 eV (532 nm) Nd:YAG laser was used as the excitation source, and the Raman emission was collected and dispersed by an 1800 gr/mm grating. The laser was focused on the exfoliated Ta₂Ni₃Te₅ flakes through a 100× objective lens (NA = 0.9, WD = 0.21 mm) with a laser spot around 1 μ m. Peak positions of Raman modes were obtained through the average peak values of multiple spectra normalized using 520 cm⁻¹ as the signal of the substrate. For polarized Raman experiments, the polarization of the incident laser was manipulated with a fixed linear polarizer and a rotating half-wave plate, while the scattered Raman signal passed through a scrambler before passing through a second polarizer, which was kept stationary. Orientation-dependent data were obtained by rotating the polarization of the incident light without the use of an analyzer. The resonance Raman effect was investigated using lasers with excitation energies of 1.58 eV (785 nm), 1.96 eV (633 nm), 2.33 eV (532 nm), 2.62 eV (473 nm), and 3.06 eV (405 nm). All Raman measurements were taken under ambient conditions. Each Raman mode was analyzed by using Gaussian-Lorentzian fittings. The angle-dependent experimental data were fitted in OriginPro using a nonlinear leastsquares fit and eqs 8 and 9 with the variables shown in Supporting Table 1 as fitting parameters.

ASSOCIATED CONTENT

Supporting Information

The Supporting Information is available free of charge at https://pubs.acs.org/doi/10.1021/acsnano.3c09527.

AFM and optical images of additional Scotch tape exfoliated $Ta_2Ni_3Te_5$ flakes, SEM images of samples exfoliated via sonication, Fourier transform of TEM images, TEM analysis, simulations, and diffraction, electron diffraction pattern of additional samples, predicted Raman fitting corresponding to Figure 5, Raman fitting for parallel configuration, fitting parameters, additional Raman spectra for parallel and crosspolarized configurations along [001] and [010] crystal directions, low-intensity peak analysis, stability of Raman signal with time, and derivation of Raman intensity equations used in the main text (PDF)

AUTHOR INFORMATION

Corresponding Authors

Humberto R. Gutiérrez — Department of Physics, University of South Florida, Tampa, Florida 33620, United States; orcid.org/0000-0001-8997-5274; Email: humberto3@usf.edu

Saiful I. Khondaker — NanoScience Technology Center and Department of Physics, University of Central Florida, Orlando, Florida 32816, United States; School of Electrical Engineering and Computer Science, University of Central Florida, Orlando, Florida 32826, United States;

orcid.org/0000-0003-1333-1928; Email: saiful@ucf.edu

Authors

- Kamal Harrison NanoScience Technology Center and Department of Physics, University of Central Florida, Orlando, Florida 32816, United States; orcid.org/0009-0005-5013-8547
- **Dylan A. Jeff** NanoScience Technology Center and Department of Physics, University of Central Florida, Orlando, Florida 32816, United States
- Jonathan M. DeStefano Department of Physics, University of Washington, Seattle, Washington 98195, United States; orcid.org/0000-0002-7220-1261
- Olivia Peek Department of Physics, University of Washington, Seattle, Washington 98195, United States
- Akihiro Kushima Department of Materials Science and Engineering, and Advanced Materials Processing and Analysis Center, University of Central Florida, Orlando, Florida 32816, United States; orcid.org/0000-0001-5166-4198
- Jiun-Haw Chu Department of Physics, University of Washington, Seattle, Washington 98195, United States

Complete contact information is available at: https://pubs.acs.org/10.1021/acsnano.3c09527

Notes

The authors declare no competing financial interest.

ACKNOWLEDGMENTS

We thank R. Sharma, F. Gonzalez, and G. De La Torre for their help. This work was supported by Grant DMR-2121953 from NSF Partnerships for Research and Education in Materials (PREM). We acknowledge the support from UW Molecular Engineering Materials Center, an NSF Materials Research Science and Engineering Center (Grant No. DMR-1719797 and DMR-2308979). This work was also supported by the Air Force Office of Scientific Research under Grant No. FA9550-21-1-0068, the David and Lucile Packard Foundation, and the Gordon and Betty Moore Foundation's EPiOS Initiative, Grant No. GBMF6759 to J.-H.C. This material is based upon work supported by the National Science Foundation Graduate Research Fellowship Program under Grant No. DGE-2140004. Any opinions, findings, and conclusions or recommendations expressed in this material are those of the authors and do not necessarily reflect the views of the National Science Foundation.

REFERENCES

- (1) Hasan, M. Z.; Kane, C. L. Colloquium: Topological insulators. *Rev. Mod. Phys.* **2010**, *82*, 3045–3067.
- (2) Nayak, C.; Simon, S. H.; Stern, A.; Freedman, M.; Das Sarma, S. Non-Abelian anyons and topological quantum computation. *Rev. Mod. Phys.* **2008**, *80*, 1083–1159.
- (3) Qi, X.-L.; Zhang, S.-C. The quantum spin Hall effect and topological insulators. *Phys. Today* **2010**, *63*, 33–38.
- (4) Murakami, S.; Nagaosa, N.; Zhang, S. C. Dissipationless quantum spin current at room temperature. *Science* **2003**, *301*, 1348–1351.
- (5) Sinova, J.; Culcer, D.; Niu, Q.; Sinitsyn, N. A.; Jungwirth, T.; MacDonald, A. H. Universal intrinsic spin Hall effect. *Phys. Rev. Lett.* **2004**, 92, No. 126603.
- (6) Kane, C. L.; Mele, E. J. Quantum spin Hall effect in graphene. *Phys. Rev. Lett.* **2005**, 95, No. 226801.
- (7) Konig, M.; Wiedmann, S.; Brune, C.; Roth, A.; Buhmann, H.; Molenkamp, L. W.; Qi, X. L.; Zhang, S. C. Quantum spin hall insulator state in HgTe quantum wells. *Science* **2007**, *318*, 766–770.

- (8) Wang, W.; Zhang, X.; Xu, H.; Zhao, Y.; Zou, W.; He, L.; Xu, Y. Evidence for Layered Quantized Transport in Dirac Semimetal ZrTe5. *Sci. Rep.* **2018**, 8, No. 5125.
- (9) Wu, C.; Bernevig, B. A.; Zhang, S. C. Helical liquid and the edge of quantum spin Hall systems. *Phys. Rev. Lett.* **2006**, *96*, No. 106401.
- (10) Lepkowski, S. P.; Bardyszewski, W. Topological insulator with negative spin-orbit coupling and transition between Weyl and Dirac semimetals in InGaN-based quantum wells. *Sci. Rep.* **2018**, *8*, No. 15403
- (11) Qian, X.; Liu, J.; Fu, L.; Li, J. Solid state theory. Quantum spin Hall effect in two-dimensional transition metal dichalcogenides. *Science* **2014**, *346*, 1344–1347.
- (12) Higashihara, N.; Okamoto, Y.; Yoshikawa, Y.; Yamakawa, Y.; Takatsu, H.; Kageyama, H.; Takenaka, K. Superconductivity in Nb2Pd3Te5 and Chemically-Doped Ta2Pd3Te5. *J. Phys. Soc. Jpn.* **2021**, *90*, No. 063705.
- (13) Wakisaka, Y.; Sudayama, T.; Takubo, K.; Mizokawa, T.; Arita, M.; Namatame, H.; Taniguchi, M.; Katayama, N.; Nohara, M.; Takagi, H. Excitonic insulator state in Ta2NiSe5 probed by photoemission spectroscopy. *Phys. Rev. Lett.* **2009**, *103*, No. 026402.
- (14) Gillet, Y.; Kontur, S.; Giantomassi, M.; Draxl, C.; Gonze, X. Ab Initio Approach to Second-order Resonant Raman Scattering Including Exciton-Phonon Interaction. *Sci. Rep* **2017**, *7*, 7344.
- (15) Mazza, G.; Rosner, M.; Windgatter, L.; Latini, S.; Hubener, H.; Millis, A. J.; Rubio, A.; Georges, A. Nature of Symmetry Breaking at the Excitonic Insulator Transition: Ta2NiSe5. *Phys. Rev. Lett.* **2020**, 124, No. 197601.
- (16) Wang, X.; Geng, D.; Yan, D.; Hu, W.; Zhang, H.; Yue, S.; Sun, Z.; Kumar, S.; Schwier, E. F.; Shimada, K.; et al. Observation of topological edge states in the quantum spin Hall insulator Ta2Pd3Te5. *Phys. Rev. B* **2021**, *104*, No. L241408.
- (17) Wang, A.; Li, Y.; Yang, G.; Yan, D.; Huang, Y.; Guo, Z.; Gao, J.; Huang, J.; Zeng, Q.; Qian, D.; et al. A robust and tunable Luttinger liquid in correlated edge of transition-metal second-order topological insulator Ta₂Pd₃Te₅. *Nat. Commun.* **2023**, *14*, 7647.
- (18) Guo, Z.; Deng, J.; Xie, Y.; Wang, Z. Quadrupole topological insulators in Ta2M3Te5 (M = Ni, Pd) monolayers. *npj Quantum Materials* **2022**, *7*, 87.
- (19) Guo, Z.; Yan, D.; Sheng, H.; Nie, S.; Shi, Y.; Wang, Z. Quantum spin Hall effect in Ta2M3Te5(M = Pd,Ni). *Phys. Rev. B* **2021**, *103*, No. 115145.
- (20) Yang, H.; Zhou, Y.; Wang, S.; Wang, J.; Chen, X.; Zhang, L.; Xu, C.; Yang, Z. Pressure-induced nontrivial Z2 band topology and superconductivity in the transition metal chalcogenide Ta2Ni3Te5. *Phys. Rev. B* **2023**, *107*, No. L020503.
- (21) Li, L.; Han, W.; Pi, L.; Niu, P.; Han, J.; Wang, C.; Su, B.; Li, H.; Xiong, J.; Bando, Y.; et al. Emerging in-plane anisotropic two-dimensional materials. *InfoMater.* **2019**, *1*, 54–73.
- (22) Luo, Z.; Maassen, J.; Deng, Y.; Du, Y.; Garrelts, R. P.; Lundstrom, M. S.; Ye, P. D.; Xu, X. Anisotropic in-plane thermal conductivity observed in few-layer black phosphorus. *Nat. Commun.* **2015**, *6*, 8572.
- (23) Wang, X.; Jones, A. M.; Seyler, K. L.; Tran, V.; Jia, Y.; Zhao, H.; Wang, H.; Yang, L.; Xu, X.; Xia, F. Highly anisotropic and robust excitons in monolayer black phosphorus. *Nat. Nanotechnol.* **2015**, *10*, 517–521.
- (24) Xia, F.; Wang, H.; Jia, Y. Rediscovering black phosphorus as an anisotropic layered material for optoelectronics and electronics. *Nat. Commun.* **2014**, *5*, 4458.
- (25) Fei, R.; Faghaninia, A.; Soklaski, R.; Yan, J. A.; Lo, C.; Yang, L. Enhanced thermoelectric efficiency via orthogonal electrical and thermal conductances in phosphorene. *Nano Lett.* **2014**, *14*, 6393–6399
- (26) Tran, V.; Soklaski, R.; Liang, Y.; Yang, L. Layer-controlled band gap and anisotropic excitons in few-layer black phosphorus. *Phys. Rev. B* **2014**, *89*, No. 235319.
- (27) Buscema, M.; Groenendijk, D. J.; Blanter, S. I.; Steele, G. A.; van der Zant, H. S.; Castellanos-Gomez, A. Fast and broadband

- photoresponse of few-layer black phosphorus field-effect transistors. *Nano Lett.* **2014**, *14*, 3347–3352.
- (28) Jain, A.; Ong, S. P.; Hautier, G.; Chen, W.; Richards, W. D.; Dacek, S.; Cholia, S.; Gunter, D.; Skinner, D.; Ceder, G.; et al. Commentary: The Materials Project: A materials genome approach to accelerating materials innovation. *APL Mater.* **2013**, *1*, No. 011002.
- (29) Momma, K.; Izumi, F. VESTA 3for three-dimensional visualization of crystal, volumetric and morphology data. *J. Appl. Crystallogr.* **2011**, *44*, 1272–1276.
- (30) Tremel, W. Isolated and Condensed Ta2Ni2 Clusters in the Layered Tellurides Ta2Ni2Te4 and Ta2Ni3Te5. *Angew. Chem.* **1991**, 103, 900–903.
- (31) Zhao, Y.; Luo, X.; Li, H.; Zhang, J.; Araujo, P. T.; Gan, C. K.; Wu, J.; Zhang, H.; Quek, S. Y.; Dresselhaus, M. S.; et al. Interlayer breathing and shear modes in few-trilayer MoS2 and WSe2. *Nano Lett.* **2013**, *13*, 1007–1015.
- (32) Pizzi, G.; Milana, S.; Ferrari, A. C.; Marzari, N.; Gibertini, M. Shear and Breathing Modes of Layered Materials. *ACS Nano* **2021**, *15*, 12509–12534.
- (33) Kroumova, E.; Aroyo, M. I.; Perez-Mato, J. M.; Kirov, A.; Capillas, C.; Ivantchev, S.; Wondratschek, H. Bilbao Crystallographic Server: Useful Databases and Tools for Phase-Transition Studies. *Phase Transitions* **2003**, *76*, 155–170.
- (34) Ribeiro, H. B.; Pimenta, M. A.; de Matos, C. J.; Moreira, R. L.; Rodin, A. S.; Zapata, J. D.; de Souza, E. A.; Castro Neto, A. H. Unusual angular dependence of the Raman response in black phosphorus. *ACS Nano* **2015**, *9*, 4270–4276.
- (35) Kranert, C.; Sturm, C.; Schmidt-Grund, R.; Grundmann, M. Raman Tensor Formalism for Optically Anisotropic Crystals. *Phys. Rev. Lett.* **2016**, *116*, No. 127401.
- (36) Michalke, H. Quantitative Untersuchungen der Polarisation der Raman-Linien von Kristallen. Z. Physik 1938, 108, 748–770.
- (37) Zhang, S.; Mao, N.; Zhang, N.; Wu, J.; Tong, L.; Zhang, J. Anomalous Polarized Raman Scattering and Large Circular Intensity Differential in Layered Triclinic ReS2. ACS Nano 2017, 11, 10366–10372.
- (38) Lorchat, E.; Froehlicher, G.; Berciaud, S. Splitting of Interlayer Shear Modes and Photon Energy Dependent Anisotropic Raman Response in N-Layer ReSe2 and ReS2. ACS Nano 2016, 10, 2752—2760.
- (39) Beams, R.; Cancado, L. G.; Krylyuk, S.; Kalish, I.; Kalanyan, B.; Singh, A. K.; Choudhary, K.; Bruma, A.; Vora, P. M.; Tavazza, F.; et al. Characterization of Few-Layer 1T' MoTe2 by Polarization-Resolved Second Harmonic Generation and Raman Scattering. ACS Nano 2016, 10, 9626–9636.
- (40) Cardona, M. Introduction. Light Scattering in Solids. *Topics in Applied Physics* **1975**, *8*, 1–22.
- (41) Berkdemir, A.; Gutiérrez, H. R.; Botello-Méndez, A. R.; Perea-López, N.; Elías, A. L.; Chia, C.-I.; Wang, B.; Crespi, V. H.; López-Urías, F.; Charlier, J.-C.; et al. Identification of individual and few layers of WS2 using Raman Spectroscopy. *Sci. Rep.* **2013**, *3*, 1755.